Journal of Applied Physics

Effect of sample anisotropy on scanning near-field optical microscope images

Cite as: J. Appl. Phys. **129**, 083105 (2021); https://doi.org/10.1063/5.0039632
Submitted: 08 December 2020 . Accepted: 05 February 2021 . Published Online: 23 February 2021

S. T. Chui, Xinzhong Chen, Ziheng Yao, Hans A. Bechtel, Michael C. Martin, G. L. Carr, and Mengkun Liu

Journal of Applied Physics ARTICLE scitation.org/journal/jap

Effect of sample anisotropy on scanning near-field optical microscope images

Cite as: J. Appl. Phys. **129**, 083105 (2021); doi: 10.1063/5.0039632
Submitted: 8 December 2020 · Accepted: 5 February 2021 ·
Published Online: 23 February 2021

View Online Export Citation CrossMark

S. T. Chui,[1,a)] Xinzhong Chen,[2] Ziheng Yao,[2,3] Hans A. Bechtel,[3] Michael C. Martin,[3] G. L. Carr,[4] and Mengkun Liu[2,4]

AFFILIATIONS

[1]Bartol Research Institute and Department of Physics and Astronomy, University of Delaware, Newark, Delaware 19716, USA
[2]Department of Physics and Astronomy, Stony Brook University, Stony Brook, New York 11790, USA
[3]Advanced Light Source Division, Lawrence Berkeley National Laboratory, Berkeley, California 94720, USA
[4]National Synchrotron Light Source, Brookhaven National Laboratory, Upton, New York 11973, USA

[a)]**Author to whom correspondence should be addressed:** chui@udel.edu

ABSTRACT

Scattering-type scanning near-field optical microscopy (s-SNOM) has been widely used to characterize strongly correlated electronic, two dimensional, and plasmonic materials, and it has enormous potential for biological applications. Many of these materials exhibit anisotropic responses that complicate the extraction of dielectric constants from s-SNOM measurements. Here, we generalize our recently developed approach for retrieving the near-field scattering signal from isotropic systems and apply it to anisotropic dielectrics. Specifically, we compare our theoretical results with experimental measurements on modestly anisotropic sapphire that exhibit strong resonances at the infrared frequency range. Good agreement with the experimental result is found. Our result is important for understanding the near-field response of low damping, anisotropic polaritonic states in dielectric media.

I. INTRODUCTION

Scattering-type scanning near-field optical microscopy (s-SNOM) has become an extremely useful tool for sample characterization during the past two decades.[1–4] The confined near-field tip-sample interaction effectively probes a sample volume in the order of $10^3\,\mathrm{nm}^3$–$10^5\,\mathrm{nm}^3$ under a metallic tip with height h, tip and base radii a and b, which enhances the incoming light. There have been extensive studies on the topic of understanding the scattered near-field signal on homogeneous samples.[5–9] A current important direction of application is to solid-state systems including strongly correlated materials,[10] two dimensional van der Waals films,[11] and most biological samples,[12] which exhibit anisotropic dielectric properties due to unidirectional lattices or structural heterogeneity. Although a model based on the point-dipole approximation for the anisotropic sample having cylindrical symmetry with respect to the normal direction of the sample has been proposed,[13,14] a rigorous theoretical treatment of the near-field signals on anisotropic materials without the cylindrical symmetry and with realistic tip geometry is still unavailable. In these systems, the near-field scattering spectrum can be quite different from its far-field counterpart where the tip-sample interaction is not present and the light momentum is effectively zero.[15]

We recently developed a first principles calculation to treat the scattering that takes into account singularities from the sharp conical tip and found better agreement with experimental results for the near field signal than those obtained with state-of-the-art numerical and analytical models.[9] Here, we generalize our result to anisotropic materials and examine situations where there is no cylindrical symmetry in the sample plane. We use sapphire (Al_2O_3), which is hexagonal and exhibits a uniaxial anisotropic dielectric tensor ($\epsilon_a = \epsilon_b \neq \epsilon_c$) in the mid-infrared (IR) regime. The near-field scattering signal and its dependence on the relative orientation between the incoming field with respect to the principal axis are calculated and compared to experiments with ultra-broadband nano-IR spectroscopy. Good agreement is found.

II. BACKGROUND

Our experimental setup is illustrated in Fig. 1. For our tip $h = 70\,\mu\mathrm{m}$, $b = 20\,\mu\mathrm{m}$, $a = 20\,\mathrm{nm}$. The incoming field is at an

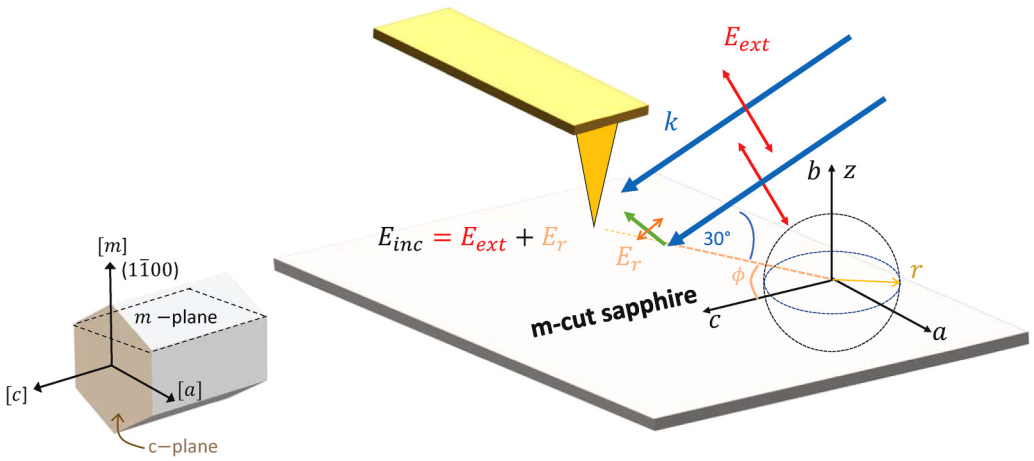

FIG. 1. Schematic representation of the scattering near-field setup. The total incident field on the tip comes from both the direct incidence and secondary surface reflection. *a*, *b*, and *c* denote the crystal axis of sapphire. The dashed line indicates the direction of the electric field in-plane components. The unit cell of sapphire is also shown with the m and *c* planes indicated. For *c*-cut sapphire, the crystal *c* axis is along *z*.

angle of 60° with respect to the sample surface normal, which we denote as the z axis. We denote the in-plane positions by cylindrical coordinates (r, ϕ). The total incoming field at the tip is a sum of the external plane waves of wave vector $\mathbf{k}$ and the reflected light from the sample, that is,

$$\mathbf{E}_{in}(r, \phi, z) = \mathbf{E}_{ext}(r, \phi)e^{ik_z z} + \mathbf{E}_r(r, \phi)e^{-ik_z z}. \quad (1)$$

The fields can be expanded in terms of cylindrical vector fields with different angular momentum m for the ϕ dependence. This total field induces a time-dependent charge Q at the atomic force microscope (AFM) tip at a distance $d = d_0(1 - \cos\Omega t) + d_m$ above the film. The AFM is operating in the tapping mode. $d_0 \sim 50$ nm is the tip oscillation amplitude. $\Omega \sim 250$ kHz is the tip oscillation frequency. $d_m \sim 1$ nm is the minimum tip-sample distance. The radiation from this charge and its image gives rise to the experimental signal. In the experiment, the electric field is in the plane of incidence (*p*-polarized). There are electric field components along the sample surface and along its normal due to the finite angle of incidence. The properties of plane waves and their reflection in anisotropic systems are described in Appendix A. The ratio of the reflected to the external field at the air-sapphire interface is given by

$$E_r/E_{ext} = \frac{k_{z1} - k_{z2}/\langle \epsilon_{plane} \rangle}{k_{z2}/\langle \epsilon_{plane} \rangle + k_{z1}}. \quad (2)$$

For m-cut (c-cut) sapphire, $\langle \epsilon_{plane} \rangle = \epsilon_c \cos^2\phi + \epsilon_a \sin^2\phi$ ($\langle \epsilon_{plane} \rangle = \epsilon_a$), ϕ is the angle between the planar component of the electric field and the crystal c-axis. In terms of the wave vector k_{plane} parallel to the plane,

$$k_{1z} = (\omega^2 - k_{plane}^2)^{1/2}.$$

For m-cut sapphires,

$$k_{2z} = (\epsilon_c\omega^2 - k_{plane}^2\langle \epsilon_{plane} \rangle/\epsilon_a)^{1/2}.$$

For c-cut sapphires,

$$k_{2z} = (\epsilon_a\omega^2 - k_{plane}^2\epsilon_a/\epsilon_c)^{1/2}.$$

The reflected light is sensitive to the orientation of the sample, which is particularly significant when close to a sharp plasmon resonance where the denominator on the right hand side of Eq. (2), $k_{z2}/\langle \epsilon_{plane} \rangle + k_{z1}$, is small [see Eq. (A4)]. Normally, the reflection coefficient is not strongly frequency dependent so its effect can be absorbed as a renormalized incoming field. For sapphire, there is a strong resonance and the effect of the reflected wave has to be explicitly included.

We describe the interaction between the tip and an anisotropic sample, which can be described in terms of an image charge. This image charge for a cylindrically symmetric anisotropic case was studied by Mele.[18] We next describe how to generalize this result for the case where there is no in-plane cylindrical symmetry. We write the electric fields in terms of their Fourier components as $\mathbf{E}(r, t) = \int d\mathbf{q}/(2\pi)^3 \mathbf{E}(q)e^{i(\mathbf{q}\cdot\mathbf{r} - \omega_q t)}$ and consider the scattering of the EM wave emitted by the tip charge from a planar sample surface with a normal in the z direction. Let the principal axis of the sample be x, y, and z with dielectric constant ϵ_i with $i = x, y, z$. The incoming EM field induces a charge Q at the AFM tip at a distance d above the sample. Similar to the isotropic case, this charge induces an image charge βQ at a distance d below the sample surface. The calculation for β for the anisotropic case is described in Appendix B. It can be obtained similar to that in the calculation of the reflection of light by matching the tangential electric and the normal displacement fields at the interface except that the

incoming field is not a plane field but that due to the point charge. We found that

$$\beta = (1 - \langle\epsilon\rangle)/(1 + \langle\epsilon\rangle), \tag{3}$$

$$\langle\epsilon\rangle = \sqrt{\langle\epsilon_{plane}\rangle\epsilon_z}. \tag{4}$$

Here, $\langle\epsilon_{plane}\rangle = \int_0^{2\pi} d\phi/(2\pi)(\epsilon_x \cos^2\phi + \epsilon_y \sin^2\phi)$. Equation (4) is in agreement with the result from the method of images in the isotropic case and in the case with cylindrical symmetry.[18] This average value $\langle\epsilon_{plane}\rangle$ is independent of the angle of the incident field because the induced charge at the tip comes from the $m = 0$ mode and is an average over all in plane directions.

We have previously investigated the scattering of EM waves from the tip using basis functions obtained from a conformal mapping between a cone and an annulus.[9] This is recapitulated in Appendix C. In our study, we find that the time-dependent signal $S(t)$ is proportional to the $m = 0$ angular component of the charge density $\sigma_{m=0}$ at the tip, which, in turn, is proportional to the incident field on the cone: $\sigma_{m=0} = tE$, where $tE = t_{m=0}E_{m=0,+k_z} + t^*_{m=0}E_{m=0,-k_z}$, for some complex function t. For our present case, the tip height is comparable to the wavelength. We have calculated[9] the function $t_{m=0}$ without making the assumption of a uniform external field. We found that the time dependent s-SNOM signal is given by[9]

$$S(t)e^{-i\omega t} \propto tE(1 + \beta)\cos(\Omega t)/[1 - \beta I(2d)]. \tag{5}$$

Here, $I(2d) = \langle E_{cz}\rangle$ is the normalized z component of the Coulomb electric field from the image charge averaged over the tip, which is at a distance $2d$ in the normal direction,

$$I(2d) = \int d\phi \int_0^{R_2} r'dr' \int_0^a rdrE_{cz}/(\pi a^2). \tag{6}$$

Here, $E_{cz} = 2d[4d^2 + r^2 + r'^2 - 2rr'\cos\phi]^{3/2}$ and R_2 is the size of the sample. In practice, for the r' integral, the contribution for $r' \gg a$ is very small. The numerical result for $I(2d)$ is shown in Fig. 2. For $2d \ll a$, $I(2d) \approx 1/2$. For $2d \gg a$, $I(2d) \approx a^2/(16d^2)$. Our numerical results agree with these limits. In our calculation, we find that the real part of $t_{m=0}$ is small. Thus, $t^*_{m=0} \approx -t_{m=0}$, $tE \approx t_{m=0}(E^{ext}_{m=0} - E^r_{m=0})$. The effect of a reflected wave has been discussed,[14] but the wave was assumed to be uniform over the tip and the different scattering of the incident and the reflected wave from the tip has not been included.

III. RESULTS

Using as input experimental values of the dielectric constants, we have studied the case of m-cut sapphire where the c-axis is in the plane of the sample. In Fig. 3, we showed the experimental (symbols) and theoretical (lines) results for the amplitude S_2 of the near-field signal demodulated at the second harmonics of the tip taping frequency as a function of incident light frequency for $\phi = 0$ and $\pi/2$. The agreement is quite good. There is some structure in the theoretical results at $\phi = 0$ at around 400 1/cm. The signal is probably too small to be resolved experimentally. We found that the dependence on ϕ comes from the dependence of the reflected field E_r on ϕ in Eq. (2). For comparison, we have also shown results using the finite dipole model[7] (FD) with two different choices of the effective dielectric constant.

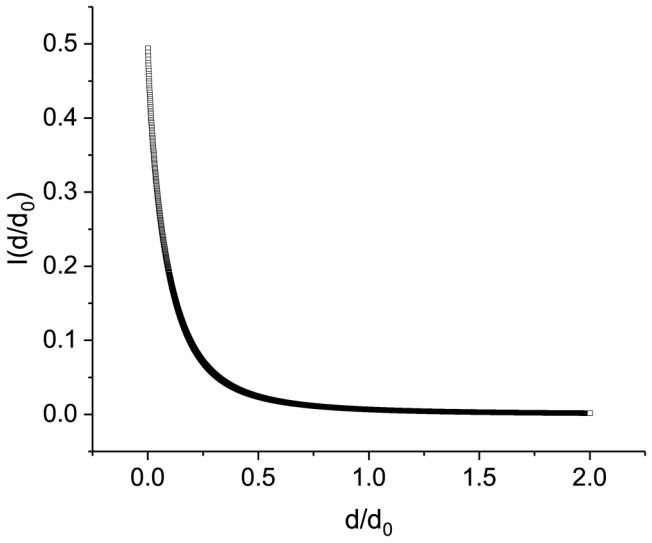

FIG. 2. Integral I as a function of the normalized distance d/d_0.

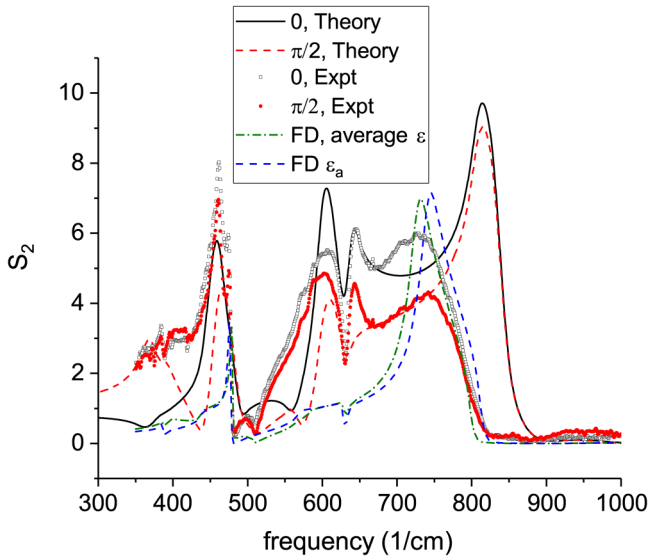

FIG. 3. Experimental and theoretical amplitude S_2 as a function of frequency for m-cut sapphire. Also shown are results for the finite dipole (FD) model with effective dielectric constants of ϵ_a and $(\epsilon_c\epsilon_a)^{1/2}$.

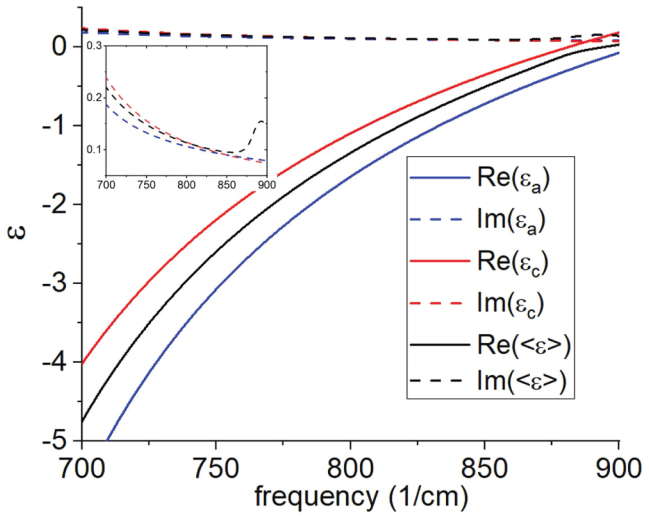

FIG. 4. Dielectric constant ϵ_a, ϵ_c, and $\langle\epsilon\rangle = \sqrt{\epsilon_a\epsilon_c}$.

At frequencies slightly above 800 1/cm, we find a peak in S_2 in Fig. 3 from our calculation. Experimentally, this peak seems to have shifted to a lower frequency. We examine the dielectric constant at frequencies where there is a disagreement between theory and experiment and find that at these frequencies in our calculation, we have used experimental dielectric constants $\epsilon \approx -1$ [and $Im(\epsilon)$ is small], which is the condition for a sharp surface plasmon resonance of large wavevector. Values of ϵ_a, ϵ_c, and $\langle\epsilon\rangle = \sqrt{\epsilon_a\epsilon_c}$ are shown in Fig. 4. The corresponding βs are shown in Fig. 5. Close to the resonance β is large.

Sapphire exhibits an effective phonon–polariton resonance, which strongly couples with the photonic states at the tip. The experimental dielectric constants used in our calculation are for long wavelengths, whereas our experimental measurement corresponds to a length of the order of the tip size. This is one possible reason that can shift the resonance frequency. Of course, our calculation can be used to extract from the experimental result what the dielectric constant really is.

We have examined other possible sources of the disagreement. We have assumed that the tip vibration is independent of the measurement but the vibration can be coupled to the surface plasmon. We have estimated the force between the induced tip charge and its image and found that it is indeed much less than the cantilever force. More precisely, the intensity of the laser is within mW range, with a focal spot of about 20μm for the laser beam. From the Poynting vector, we found that the external EM field E_{ext} is thus of the order of 14×10^3 V/m. From this, we can estimate the induced charge Q at the tip and the average force between the tip and its image $F_E = \langle Q^2/(4\pi\epsilon_0 r^2)\rangle$. We get $F_E \approx 10^{-3}$ pN. This estimate is much less than the force on the cantilever, which is in the pN range.

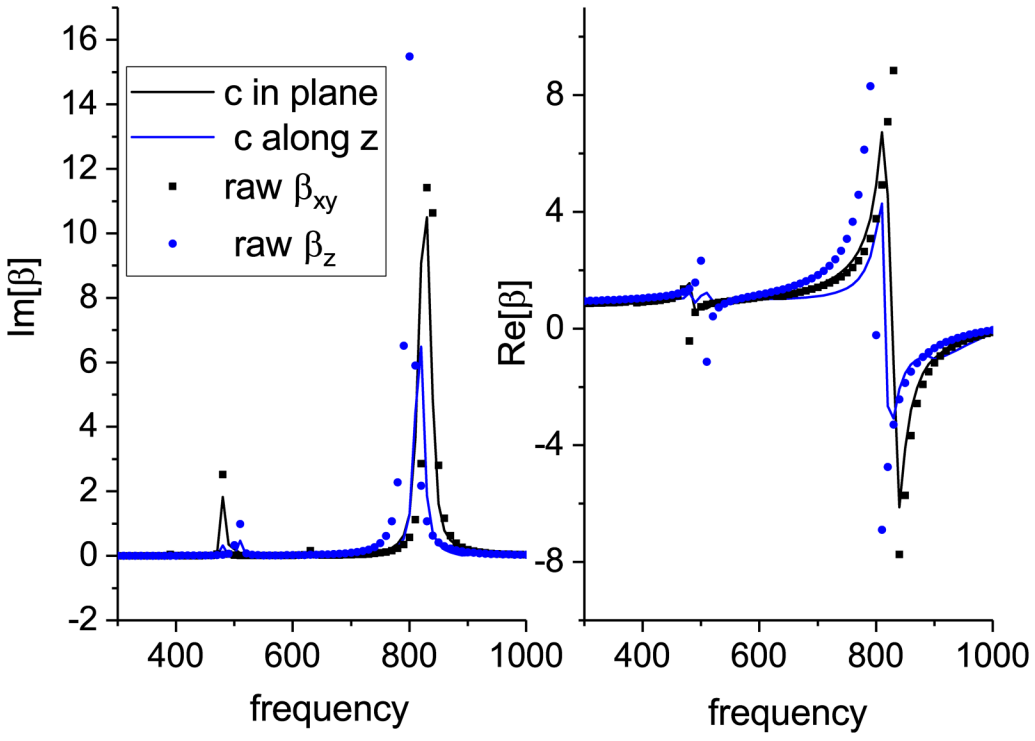

FIG. 5. The response function β for the dielectric constant in Fig. (4). Also shown are values of β for c cut sapphire where the geometric mean in Eq. (4) is not taken. These curves are labeled as raw.

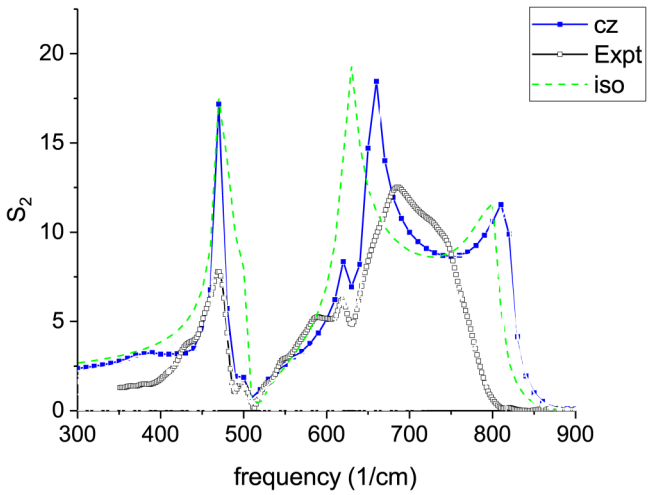

FIG. 6. Experimental and theoretical S_2 as a function of frequency for c-cut sapphire with the average anisotropic dielectric constant $\langle\epsilon\rangle = \sqrt{\epsilon_a\epsilon_c}$ for β and with one of the components of the dielectric constant ϵ_c alone ("iso").

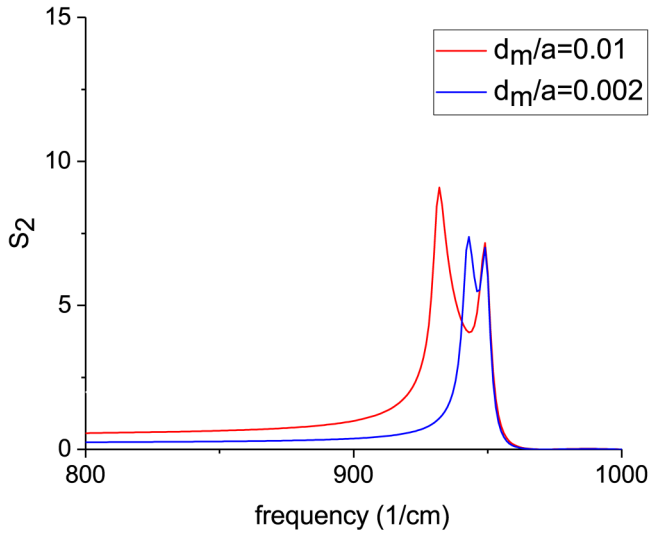

FIG. 7. S_2 for s-SNOM as a function of frequency for SiC for different minimum tip height in units of the tip radius.

A. Minimum tip height dependence

A fitting parameter in our calculation is the minimum distance of the tip above the sample, d_m. We found that our result can change as this value is changed. Physically, in Eq. (5), if the imaginary part of β is small and *the real part is sufficiently large*, the denominator on the right hand side can become zero as β approaches $1/I(2d)$. The value of d_m determines when this occurs.

In Fig. 6, we show experimental results for the amplitude S_2 of the near-field signal demodulated at the second harmonics of the tip taping frequency as a function of incident light frequency for the c-cut sapphire obtained in an earlier experiment. Also shown is the theoretical result labeled as "cz" we obtained using ϵ from Eq. (4) and a minimum height different from that in the study of the m-cut case. We have also computed S_2 for isotropic media using the dielectric constant along the c-axis. The result is shown as the graph "iso" in Fig. 6. The agreement with the experiment result is better for the curve "cz."

The dependence of the s-SNOM signal on tip-sample distance has been reported by Wang and co-workers[19] on SiC. We have explored possible dependence of the s-SNOM signal on d_m for SiC. Our result for S_2 for s-SNOM as a function of frequency for SiC for different minimum tip-sample distances is shown in Fig. 7 and is similar to Fig. 4(b) of Ref. 19.

In conclusion, we extend our recent theoretical investigation of the s-SNOM signal to anisotropic dielectrics and compare the results with experimental measurements on modestly anisotropic m-cut and c-cut sapphire that exhibit strong resonances at the IR frequency range. Improved agreement with the experimental result is found. The dependence on the orientation of the sample comes from the reflection of the incoming light from the sample onto the scattering tip. Our result depends on the minimum distance of the tip from the sample. It is important for understanding the near-field response of low damping, anisotropic polaritonic states in dielectric media.

ACKNOWLEDGMENTS

We acknowledge support from the National Science Foundation under Grant No. DMR-1904576. This work was partly supported by the RISE2 node of NASA's Solar System Exploration Research Virtual Institute under NASA Cooperative Agreement No. 80NSSC19MO2015. We also acknowledge the helpful discussions with Lukas Wehmeier. This research used resources of the Advanced Light Source, a U.S. DOE Office of Science User Facility under Contract No. DE-AC02-05CH11231. Z.Y. acknowledges the partial support from the ALS Doctoral Fellowship in Residence Program.

APPENDIX A: PLANE WAVE AND REFLECTION IN ANISOTROPIC SYSTEMS

In this appendix, we consider the dispersion of a plane wave and its reflection in anisotropic systems. Maxwell's equations for the plane wave can be written in terms of its wave vector in matrix form as

$$\mathbf{\Omega E} = 0, \tag{A1}$$

where $\mathbf{\Omega}_{ij} = (k^2\delta_{ij} - k_ik_j) - \omega^2\delta_{ij}\epsilon_i$. For m-cut sapphires with their c axis along x, from $\nabla \cdot D = 0$, we get $\epsilon_{ab}(k_yE_y + k_zE_z) = -k_x\epsilon_cE_x$. By substituting this into the x component of the wave equation (A1), we get

$$\begin{aligned} &-k_x(k_x - k_x\epsilon_c/\epsilon_{ab})E_x = (\omega^2\epsilon_c - k^2)E_x,\\ &(k_y^2 + k_z^2)/\epsilon_c + k_x^2/\epsilon_{ab} = \omega^2,\\ &k_z^2 = \epsilon_c\omega^2 - k_x^2\epsilon_c/\epsilon_{ab} - k_y^2. \end{aligned} \tag{A2}$$

When ϕ is the angle between k_{plane} and the x axis,

$$k_z^2 = \epsilon_c\omega^2 - k_{plane}^2(\cos^2(\phi)\epsilon_c + \epsilon_{ab}\sin^2\phi)/\epsilon_{ab}.$$

For c-cut sapphire with the c axis along z, from $\nabla \cdot D = 0$, we get $\epsilon_{ab}(k_yE_y + k_xE_z) = -k_z\epsilon_cE_z$. By substituting this into the z component of the wave equation (A1), we get

$$\begin{gathered}-k_z(k_z - k_z\epsilon_c/\epsilon_{ab})E_z = (\omega^2\epsilon_c - k^2)E_z,\\ (k_y^2 + k_x^2)/\epsilon_c + k_z^2/\epsilon_{ab} = \omega^2.\end{gathered} \tag{A3}$$

1. Reflection

In the isotropic case,[16] the ratio of the reflected and the incident field for p polarized wave is given by

$$E_r/E_i = \frac{\epsilon_2k_{1z} - \epsilon_1k_{2z}}{\epsilon_2k_{1z} + \epsilon_1k_{2z}}.$$

The denominator is zero when

$$\begin{gathered}(\epsilon_1\omega^2 - k_{plane}^2)/\epsilon_1^2 = (\epsilon_2\omega^2 - k_{plane}^2)/\epsilon_2^2,\\ \omega^2(1/\epsilon_1 - 1/\epsilon_2) = k_{plane}^2(1/\epsilon_1^2 - 1/\epsilon_2^2),\\ \omega^2 = k_{plane}^2(1/\epsilon_1 + 1/\epsilon_2).\end{gathered} \tag{A4}$$

We recover the surface plasmon dispersion.[17] This can be generalized to anisotropic systems.

We consider the reflection of the EM wave from air (labeled by subscript 1) into the anisotropic system (subscript 2). The incident and the reflected wave are denoted by additional subscripts of $+$ and $-$. We get, from $\nabla \cdot \mathbf{D} = 0$, $k_{x1}D_{x1} + k_{y1}D_{y1} + k_{zi}(D_{z1+} - D_{z1-}) = 0$. In terms of the electric field, this becomes

$$E_{z1+} - E_{z1-} = -k_{plane}E_{plane}/k_{z1}. \tag{A5}$$

Inside the sapphire, we have $k_{x2}D_{x2} + k_{y2}D_{y2} + k_{z2}D_{z2} = 0$. If the field is in the plane of incidence, in terms of the electric field, we get for m-cut sapphires

$$E_{z2} = -k_{plane}\langle\epsilon\rangle E_{plane}/(k_{z2}\epsilon_{ab}),$$

where $\langle\epsilon_{plane}\rangle = \cos^2\phi\epsilon_c + \sin^2\phi\epsilon_{ab}$. For c-cut sapphires, we get

$$E_{z2} = -k_{plane}\epsilon_{ab}E_{plane}/(k_{z2}\epsilon_c).$$

Note that because the component of the electric field tangential to the surface is continuous, E_{plane} is the same on both sides. Combining with Eq. (A5), we get for m-cut sapphires

$$E_{z1+} - E_{z1-} = k_{z2}\epsilon_{ab}E_{z2}/k_{z1}/\langle\epsilon_{plane}\rangle \tag{A6}$$

and

$$E_{z1+} - E_{z1-} = k_{z2}\epsilon_cE_{z2}/k_{z1}/\epsilon_{ab} \tag{A7}$$

for c-cut sapphires.

Continuity of D_z implies for m-cut sapphires

$$E_{z1+} + E_{z1-} = \epsilon_{ab}E_{z2} \tag{A8}$$

and for c-cut sapphires,

$$E_{z1+} + E_{z1-} = \epsilon_cE_{z2}. \tag{A9}$$

Eliminating E_{z2}, we get for m-cut sapphires

$$E_{z1+} - E_{z1-} = k_{z2}(E_{z1+} + E_{z1-})/k_{z1}/\langle\epsilon_{plane}\rangle$$

and for c-cut sapphires,

$$E_{z1+} - E_{z1-} = k_{z2}(E_{z1+} + E_{z1-})/k_{z1}/\epsilon_{ab}.$$

This gives the ratio of the reflected to the incident electric field for m-cut sapphires given in Eq. (2),

$$E_r/E_{ext} = E_{z1-}/E_{z1+} = \frac{k_{z1} - k_{z2}/\langle\epsilon_{plane}\rangle}{k_{z2}/\langle\epsilon_{plane}\rangle + k_{z1}} \tag{A10}$$

and for c-cut sapphires,

$$E_r/E_{ext} = E_{z1-}/E_{z1+} = (k_{z1} - k_{z2}/\epsilon_{ab})/(k_{z2}/\epsilon_{ab} + k_{z1}). \tag{A11}$$

The resonance condition when the denominator is zero for m-cut sapphires is given by

$$k_{z2}/\langle\epsilon_{plane}\rangle + k_{z1} = 0.$$

This can be written as

$$\omega^2[\epsilon_{ab}/\langle\epsilon_{plane}\rangle^2 - 1) = k_{plane}^2[1/(\langle\epsilon_{plane}\rangle\epsilon_c) - 1].$$

APPENDIX B: IMAGE CHARGE IN ANISOTROPIC SYSTEMS

In this section, we describe the detail of our study of the interaction between a point charge and an anisotropic dielectric. We consider the scattering of the EM field from the tip charge by a planar sample surface with a normal in the z direction. Let the principal axis of the sample be x, y, and z with dielectric constant ϵ_i with $i = x, y, z$.

The incoming EM field induces a charge Q at the AFM tip at a distance d above the sample. For an isotropic system, this charge induces an image charge βQ with

$$\beta = (\epsilon - 1)/(\epsilon + 1),$$

at a distance d below the surface of the sample. We write the electric potential in terms of their Fourier components as $V(r, t) = \int d\mathbf{q}/(2\pi)^3V(q)e^{i(\mathbf{q}\cdot\mathbf{r} - \omega_q t)}$. After the q_z integration in the present anisotropic case, the potential due to the charge at the tip is still

$$V(r, z) = Q\pi\int d^2qe^{(-q|d-z| + iq\cdot r)}/q.$$

The scattered field can be written as that due to an image potential as

$$V_b(r, z) = \pi \int d^2qF(q)e^{(-qz+iq\cdot r)}/q$$

in terms of a function F to be determined by the boundary conditions. Inside the dielectric Coulomb's law states $\nabla \cdot D = \rho/\epsilon_0$. In the Fourier space, the corresponding potential can be written in terms of a function $K'(q)$ as $V = \int d^3qe^{iq\cdot r}K'/[q^2\langle\epsilon_{plane}\rangle + q_z^2\epsilon_z]$. We can do the q_z integration and obtain, in terms of a function $K(q)$,

$$V^<(r, z) = \pi \int d^2qK(q)e^{(q[\langle\epsilon_{plane}\rangle/\epsilon_z]^{0.5}z+iq\cdot r)}/q.$$

$\langle\epsilon_{plane}\rangle = \epsilon_x \cos^2\phi + \epsilon_y \sin^2\phi$. From the continuity of the tangential component of $\mathbf{E}$ we get $V_b + V = V^<$. This implies

$$F + Q' = K, \tag{B1}$$

where $Q' = Q\exp(-qd)$. From the continuity of D_z, we get

$$F(1 + \langle\epsilon\rangle) = Q'(1 - \langle\epsilon\rangle), \tag{B2}$$

where

$$\langle\epsilon\rangle = \sqrt{\langle\epsilon_{plane}\rangle\epsilon_z}. \tag{B3}$$

F can be interpreted as the image potential due to an image charge βQ at $\mathbf{r}_i = -d\mathbf{e}_z$, where

$$\beta = (1 - \langle\epsilon\rangle)/(1 + \langle\epsilon\rangle). \tag{B4}$$

After the angular integration over the direction of the wave vector is carried out, we arrive at the expression quoted in the text.

APPENDIX C: OUR APPROACH

We recapitulate our approach of calculating the s-SNOM signal in this appendix. We are interested in the current flow on a finite surface caused by an external electromagnetic (EM) wave. We assume that the surface of the cone to be a film that is thin enough that there is no current in the direction perpendicular to it. The current density $\mathbf{j}$ in the presence of an external electric field $\mathbf{E}_{ext}$ is governed by the equation

$$\rho\mathbf{j} + \mathbf{E}_{em} = \mathbf{E}_{ext}. \tag{C1}$$

where ρ is the resistivity, $\mathbf{E}_{em}$ is the electromagnetic field generated by the current. $\mathbf{E}_{em}$ can be obtained from the integral form of Maxwell's equation. It is a sum of a capacitive and an inductive term: $\mathbf{E}_{em} = \mathbf{E}_c + \mathbf{E}_L$. For a time dependence of $e^{i\omega t}$ these terms can be expressed in terms of the current density as

$$\mathbf{E}_C = i/(\omega\epsilon_0)\nabla \int d\mathbf{r}'G(r - r')\nabla' \cdot \mathbf{j}(r'), \tag{C2}$$

$$\mathbf{E}_L = -i\mu_0\omega \int d\mathbf{r}'\mathbf{j}(r')G(r - r'), \tag{C3}$$

where the bare Green's function G is given by

$$G = \exp(ik_0|r - r'|)/4\pi|r - r'|. \tag{C4}$$

In the quasi-static limit, the radiative correction is not included, G is approximated by $G' = 1/4\pi|r - r'|$.

We impose the boundary condition of no current flow perpendicular to the boundary of the film with a large boundary resistivity ρ_s which we take to approach infinity. The total resistivity ρ is a sum of this surface term and a metal resistivity ρ_0. Because of the surface resistivity, the normal surface current densities j_s approaches zero. We define boundary electric fields $\mathbf{E}_s = \mathbf{j}_s\rho_s$ as the products of the normal components of the current at the boundaries j_s and ρ_s. They behave like Lagrange multipliers. Their values are determined from the condition that the normal boundary currents become zero. Physically, as the external field is applied, the current is stopped at the boundary and charges of surface density σ_s are getting accumulated. An electric field is generated until it reaches a value that adds up with other external fields to oppose further current arriving there.

For the cone, there are two boundaries, the base and the tip. We call the surface field at the tip in the direction of the cone axis E_{s2}. This field is completely determined by the incoming field at the cone and the boundary condition of zero current. In the presence of an additional surface such as sapphire, the boundary field E_{s2} is now a sum of a field E_{sa} from the surface charge of density σ_s at the tip and a field E_{sb} from the image charge density. $-\beta\sigma_{s2}$ at a distance $-d$ below the surface,

$$E_{s2} = E_{sa} + E_{sb}. \tag{C5}$$

From Gauss's law $E_{sa} = \sigma_s/2\epsilon_0$, $E_{sb} \approx -\beta\sigma_s I(2d)/\epsilon_0$, where I defined in Eq. (6) is the averaged field at the tip from the image charge. From Eq. (C5), we get

$$\sigma_s = 2\epsilon_0 E_{s2}/[1 - 2\beta I(2d)]. \tag{C6}$$

In our formulation, the surface field is determined from the zero normal surface current condition, the tip charge density is then determined from the surface field. It is the tip charge density that determines the modulated scattered far field that is measured experimentally and shown in Eq. (5).

1. Solution

In our approach, we represent the currents and the fields of interest **not** in terms of finite elements on a mesh but in terms of a complete set of orthonormal basis functions. As we discussed before,[20,21] the impedance matrix becomes nearly diagonal and the convergence is very fast. For very simple cases, the basis functions are the well known special functions. For a given finite surface, there is a harmonic conformal map that maps it into an annulus with the corresponding genus.[23] We construct the basis function

for this surface from the basis function of a circular annulus with the conformal harmonic map.

The electromagnetic field $\mathbf{E}_{em}$ can be represented as $\mathbf{E}_{em} = \mathbf{Z}^{0j}$, where the "impedance" matrix $\mathbf{Z}^0$ is just the representation of the Green's function in this basis. More specifically,

$$\mathbf{Z}^0 = -i\omega\mathbf{L} - ic^2/(\omega\mathbf{C}), \tag{C7}$$

where for any basis function $\mathbf{X}$, $\mathbf{Y}$,

$$L_{Xi,Yj} = \mu_0 \int d\mathbf{r}d\mathbf{r}'[\mathbf{X}_i(r)]^* \cdot \mathbf{Y}_j(r')G(r, r') \tag{C8}$$

$$(1/C)_{Xi,Yj} = \int d\mathbf{r}d\mathbf{r}'[\mathbf{X}_i(r)]^* \cdot \nabla\nabla' \cdot \mathbf{Y}_j(r')G(r, r'). \tag{C9}$$

We found that when the basis functions are orthonormal, the off-diagonal elements of the impedance matrix is much less than the diagonal one.[20,21] Furthermore, the magnitude of the impedance increases rapidly. These greatly facilitate the convergence of the solution and provide for a much better understanding of the physics.

In this notation, the circuit equation becomes

$$\mathbf{Zj} = \mathbf{E}_{ext} + \mathbf{E}_s, \tag{C10}$$

where $Z = Z^0 + \rho_0$. We next discuss the construction of the new basis states for the cone.

2. Basis functions

A point on the cone is characterized by its angular coordinates r and ϕ, whereas a point inside the annulus is characterized by the cylindrical coordinate R and Φ. Mapping between cones and disks was studied in the context of map construction.[22] We generalized this approach and found that the above two surfaces can be mapped into each other via a conformal harmonic map,

$$R = r^{1/\sin\theta}, \quad \Phi = \phi.$$

Under this transformation, the distance on the cone $dr^2/\sin^2\theta + d\phi^2 r^2$ can be written as

$$ds^2 = R^{2\sin\theta-2}(dR^2 + R^2 d\Phi^2).$$

The Jacobian of the transformation is thus given by $\rho = R^{2\sin\theta-2}$. As expected, the Jacobian exhibits a divergence at $R = 0$.

With the circular annulus basis functions denoted by $\mathbf{X}$, we construct with functions α and β orthonormal vector basis functions on the cone given by

$$\mathbf{cX} = \alpha X_r[\mathbf{R}(\mathbf{r})]\mathbf{e}_1 + \beta X_\Phi \mathbf{e}_2, \tag{C11}$$

where the tangent vectors on the surface of the cone are in the cylindrical basis (r, ϕ, z): $\mathbf{e}_1 = 1/(1+h^2)^{1/2}\mathbf{e}_r - h/(1+h^2)^{1/2}\mathbf{e}_z$, $\mathbf{e}_2 = \mathbf{e}_\phi$. To obtain an orthonormal basis, the requirement is that $\alpha = \beta = 1/\rho^{1/2}$, where ρ is the Jacobian of the transformation. With this choice, the new basis functions are orthonormal with the corresponding measure,

$$\int d^2 r(\mathbf{cX_n})^* \cdot \mathbf{cY_m} = \int d^2 R\rho|\alpha|^2 \mathbf{X_n} \cdot \mathbf{Y_m} = \delta_{X,Y}.$$

DATA AVAILABILITY

The data that support the findings of this study are available from the corresponding author upon reasonable request.

REFERENCES

[1]M. Liu, A. J. Sternbach, and D. N. Basov, Rep. Prog. Phys. **80**, 014501 (2017).
[2]R. Hillenbrand, B. Knoll, and F. Keilmann, J. Microsc. **202**, 77 (2001).
[3]X. Chen, D. Hu, R. Mescall, G. You, D. N. Basov, Q. Dai, and M. Liu, Adv. Mater. **31**, 1804774 (2019).
[4]J. M. Atkin, S. Berweger, A. C. Jones, and M. B. Raschke, Adv. Phys. **61**, 745 (2012).
[5]A. S. McLeod, P. Kelly, M. D. Goldflam, Z. Gainsforth, A. J. Westphal, G. Dominguez, M. H. Thiemens, M. M. Fogler, and D. N. Basov, Phys. Rev. B **90**, 085136 (2014).
[6]B.-Y. Jiang, L. M. Zhang, A. H. Castro Neto, D. N. Basov, and M. M. Fogler, J. Appl. Phys. **119**, 054305 (2016).
[7]A. Cvitkovic, N. Ocelic, and R. Hillenbrand, Opt. Express **15**, 8550 (2007).
[8]B. Knoll and F. Keilmann, Opt. Commun. **182**, 321 (2000).
[9]S. T. Chui, X. Chen, M. Liu, Z. Lin, and J. Zi, Phys. Rev. B **97**, 081406(R) (2018).
[10]See, for example, A. S. McLeod, J. Zhang, M. Q. Gu, F. Jin, G. Zhang, K. W. Post, X. G. Zhao, A. J. Millis, W. B. Wu, J. M. Rondinelli, R. D. Averitt, and D. N. Basov, Nat. Mater. **19**, 397 (2020); X. Chen, X. Fan, L. Li, N. Zhang, Z. Niu, T. Guo, S. Xu, H. Xu, D. Wang, H. Zhang, A. S. McLeod, Z. Luo, Q. Lu, A. J. Millis, D. N. Basov, M. Liu, and C. Zeng, Nat. Phys. **16**, 631 (2020); C. Chen, S. Chen, R. P. S. M. Lobo, C. Maciel-Escudero, M. Lewin, T. Taubner, W. Xiong, M. Xu, X. Zhang, X. Miao, P. Li, and R. Hillenbrand, ACS Photonics **7**, 3499 (2020).
[11]See, for example, M. E. Berkowitz, B. S. Y. Kim, G. Ni, A. S. McLeod, C. F. B. Lo, Z. Sun, G. Gu, K. Watanabe, T. Taniguchi, A. J. Millis, J. C. Hone, M. M. Fogler, R. D. Averitt, and D. N. Basov, Nano Lett. **21**, 308–316 (2020); G. Hu, Q. Ou, G. Si, Y. Wu, J. Wu, Z. Dai, A. Krasnok, Y. Mazor, Q. Zhang, Q. Bao, C.-W. Qiu, and A. Alù, Nature **582**, 209 (2020); W. Ma, P. Alonso-González, S. Li, A. Y. Nikitin, J. Yuan, J. Martín-Sánchez, J. Taboada-Gutiérrez, I. Amenabar, P. Li, S. Vélez, C. Tollan, Z. Dai, Y. Zhang, S. Sriram, K. Kalantar-Zadeh, S.-T. Lee, R. Hillenbrand, and Q. Bao, Nature **562**, 557 (2018); M. Chen, X. Lin, T. H. Dinh, Z. Zheng, J. Shen, Q. Ma, H. Chen, P. Jarillo-Herrero, and S. Dai, Nat. Mater. **19**, 1307–1311 (2020).
[12]See, for example, K. Moon, Y. Do, H. Park, J. Kim, H. Kang, G. Lee, J.-H. Lim, J.-W. Kim, and H. Han, Sci. Rep. **9**, 16915 (2019); B. T. O'Callahan, M. Hentschel, M. B. Raschke, P. Z. El-Khoury, and A. S. Lea, J. Phys. Chem. C **123**, 17505–17509 (2019); Z. Yang, D. Tang, J. Hu, M. Tang, M. Zhang, H. Cui, L. Wang, C. Chang, C. Fan, J. Li, and H. Wang, Small, online version 2005814 (2020); W. Lee, Z. Zhou, X. Chen, N. Qin, J. Jiang, K. Liu, M. Liu, T. H. Tao, and W. Li, Nat. Nanotechnol. **15**, 941 (2020).
[13]S. Schneider, J. Seidel, S. Grafström, L. M. Eng, S. Winnerl, D. Stehr, and M. Helm, Appl. Phys. Lett. **90**, 143101 (2007).
[14]S. C. Schneider, S. Grafström, and L. M. Eng, Phys. Rev. B **71**, 115418 (2005); S. C. Kehr, M. Cebula, O. Mieth, T. Hartling, J. Seidel, S. Grafström, L. M. Eng, S. Winnerl, D. Stehr, and M. Helm, Phys. Rev. Lett. **100**, 256403 (2008).
[15]R. Hillenbrand, T. Taubner, and F. Keilmann, Nature **418**, 159 (2002).
[16]See, for example, R. P. Feyman, *Lectures on Physics* (Wiley, 2005), Vol. 2, Eq. (33.53).

[17]See, for example W. L. Barnes, A. Dereux, and T. W. Ebbesen, Nature **424**, 825 (2003).
[18]E. J. Mele, Am. J. Phys. **69**, 557 (2001).
[19]H. Wang, L. Wang, D. S. Jakob, and X. G. Xu, Nat. Commun. **9**, 2005 (2018).
[20]S. T. Chui and L. Zhou, *Electromagnetic Behaviour of Metallic Wire Structures* (Springer, 2013).
[21]S. T. Chui, J. J. Du, and S. T. Yau, Phys. Rev. E **90**, 053202 (2014).
[22]J. H. Lambert,*Anmerkungen und Zustze zur Entwerfung der Land- und Himmelscharten* (University of Michigan, 1772) [Translated and introduced by W. R. Tobler, *Notes and Comments on the Composition of Terrestrial and Celestial Maps* (ESRI Press, 1972), ISBN 978-1-58948-281-4]; S.T. Chui (unpublished).
[23]D. Gu and S. T. Yau, "Electromagnetic scattering from cones," in *Computational Conformal Geometry* (International Press, Boston, 2008).